

## A minimal longitudinal dynamic model of a tailless flapping wing robot for control design

Kajak, K. M.; Karásek, M.; Chu, Q. P.; de Croon, G. C.H.E.

**DOI**

[10.1088/1748-3190/ab1e0b](https://doi.org/10.1088/1748-3190/ab1e0b)

**Publication date**

2019

**Document Version**

Accepted author manuscript

**Published in**

Bioinspiration & biomimetics

**Citation (APA)**

Kajak, K. M., Karásek, M., Chu, Q. P., & de Croon, G. C. H. E. (2019). A minimal longitudinal dynamic model of a tailless flapping wing robot for control design. *Bioinspiration & biomimetics*, 14(4), Article 046008. <https://doi.org/10.1088/1748-3190/ab1e0b>

**Important note**

To cite this publication, please use the final published version (if applicable). Please check the document version above.

**Copyright**

Other than for strictly personal use, it is not permitted to download, forward or distribute the text or part of it, without the consent of the author(s) and/or copyright holder(s), unless the work is under an open content license such as Creative Commons.

**Takedown policy**

Please contact us and provide details if you believe this document breaches copyrights. We will remove access to the work immediately and investigate your claim.

# A minimal longitudinal dynamic model of a tailless flapping wing robot for control design

K.M. Kajak\*, M. Karásek†, Q.P. Chu‡, G.C.H.E. de Croon§  
Delft University of Technology, Kluyverweg 1, The Netherlands

## ABSTRACT

Recently, several insect- and hummingbird-inspired tailless flapping wing robots have been introduced. However, their flight dynamics, which are likely to be similar to that of their biological counterparts, remain yet to be fully understood. We propose a minimal dynamic model that is not only validated with experimental data, but also able to predict the consequences of various important design changes. Specifically, the model captures the flapping-cycle-averaged longitudinal dynamics, considering the main aerodynamic effects. We validated the model with flight data captured with a tailless flapping wing robot, the DelFly Nimble, for air speeds from near-hover flight up to 3.5 m/s. Moreover, the model succeeds in predicting the effects of changes to the center of mass location, and to the control system gains. Hence, the model is suitable even for the initial control design phase. To demonstrate this, we have used the simulation model to tune the robot's control system for higher speeds. Using the new control parameters on the real robot improved its maximal stable speed from 4 m/s to 7 m/s.

## 1 INTRODUCTION

Flapping wing flight remains rare in the context of man-made aircraft, but it is the only form of powered flight among biological fliers. It may be an attractive solution for small-scale micro air vehicles (MAVs). At these scales, fixed wings are impractical, as they need to maintain a relatively high speed to generate enough lift. Flapping wings offer, just like rotorcraft, a combination of hovering ability with flight in any direction. In comparison to rotorcraft, flapping wing designs are expected to be more energy efficient in forward flight, and allow further miniaturisation in future. Several of the pioneering man-made designs have used aerodynamic dampers to achieve passive stability [1, 2, 3, 4], but tailless designs are more desirable due to their potentially higher agility. Examples of working tailless designs can be found in [5, 6, 7, 8, 9].

\*Email address: karlmartin.kajak@gmail.com

†Email address: m.karasek@tudelft.nl

‡Email address: q.p.chu@tudelft.nl

§Email address: g.c.h.e.decroon@tudelft.nl

This is the version of the article before peer review or editing, as submitted by an author to Bioinspiration & Biomimetics. IOP Publishing Ltd is not responsible for any errors or omissions in this version of the manuscript or any version derived from it. The Version of Record is available online at <https://doi.org/10.1088/1748-3190/ab1e0b>.

The agility of tailless designs comes at the cost of inherent instability, requiring an active control system and a wing actuation system that can provide stabilizing control moments [10, 11, 12, 13, 14].

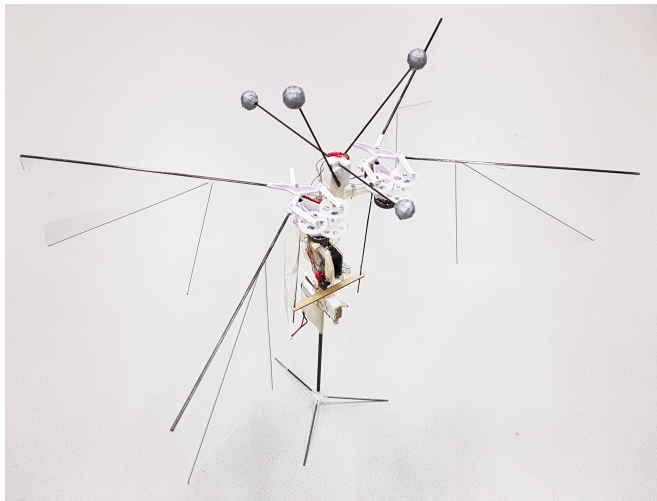


Figure 1: The DelFly Nimble tailless flapping wing robot used for model validation. Its parameters are summarized in Table 1.

In order to design such a control system, models of flapping flight dynamics would be of great use. However, due to the complexity of flapping wing aerodynamics, the existing flight dynamics models are mostly theoretical and often include numerous parameters that need to be identified for each specific animal or robot. Some works utilize computer fluid dynamic (CFD) simulations, e.g. [15, 16, 13, 17], which provide highly detailed information on the flow evolution. First attempts have even been made to model the complex fluid-structure interaction when considering the wing flexibility [18, 19]. However, setting up and running such simulations is costly in terms of time and effort.

A very popular approach is the use of quasi-steady models, relying on force coefficients obtained either empirically [20, 21, 22, 23] or derived entirely from first principles [24, 25]. In these models, to reduce simulation times, analytic formulas are used to estimate instantaneous wing forces that are treated as independent from their time history. These models have also been used with flexible wings [26]. In both CFD and quasi-steady aerodynamic models, the wing typically follows prescribed 3D wing kinematics and the forces

are resolved with fine temporal resolution. However, for subsequent stability and control analysis, the model is typically reduced via cycle averaging, a rigid-body assumption and linearization [27, 28, 29, 19].

There is yet a simpler class of models, modeling directly the average aerodynamic forces as linear damping with respect to body velocities [30, 3, 31, 9]. Although being a rough approximation of the otherwise complex aerodynamics, these models are attractive as they describe the dominant cycle-averaged effects with a minimal number of parameters. While models from all the three classes (CFD, quasi-steady, linear damping) have been employed for stability analysis and control design in simulation, e.g. [27, 29, 17, 19], so far, only [9] shows validation with real flight data, though limited to oscillations around the hover condition. Due to the lack of validation, these models could only provide general insights to the robot flight dynamics but, to our knowledge, none of the existing models have explicitly been used in the design phase of its control system (i.e. gain tuning), while this is one of the main goals of such models.

In this work, we propose a minimal model of the longitudinal dynamics of a tailless flapping wing robot based on the linear damping model. The highly reduced aerodynamic model, which models only the flapping-cycle-averaged effects, makes it applicable to any flapping wing flyers, regardless of the number of wings, their design and configuration (conventional vs X-type), dimensions and kinematics. We validate the model with flight data captured with the *DelFly Nimble* tailless flapping wing robot [32] with X-type wings (Figure 1), at flight conditions between hover (0 m/s) and forward flight (3.5 m/s), for different center of mass locations, and for different controller parameters. Furthermore, we use the model to improve the performance of the robot’s control system so that it can fly stably even at high speeds (up to 7 m/s).

The paper is organized in three parts. Section 2 presents the experimental setup utilized in the course of the validation campaign. Section 3 presents the structure of the developed dynamic model, identification of the actuator dynamics and validation of the open loop model. Section 4 introduces the controller architecture, describes the closed loop model validation procedure and results, and, finally, the model is used to improve the flight controller of the robot.

## 2 EXPERIMENTAL SETUP

The flapping wing robot used for flight tests is the *DelFly Nimble* [32] shown in Figure 1. Its main parameters are summarized in Table 1. As previous *DelFly* designs [33], it employs the X-wing concept where the two wing pairs flap in opposition. This solution enhances the produced thrust by the clap-and-peel effect and, at the same time, minimizes the resultant reaction force on the body, as the approximately identical drag forces of individual wings, acting in opposite directions, cancel out. However, unlike its predecessors, the

Table 1: *DelFly Nimble* parameters.

Parameter	Value
Wing span	0.33 m
Wing length	0.14 m
Chord length	0.088 m
Number of wings	4
Flapping amplitude	44°
Flapping frequency (hover, max.)	17 Hz, 22 Hz
Maximum speed	7 m/s
Battery capacity	180 mAh @ 3.7 V
Battery life (hover)	5 minutes
Weight (inc. tracking markers)	29.4 g

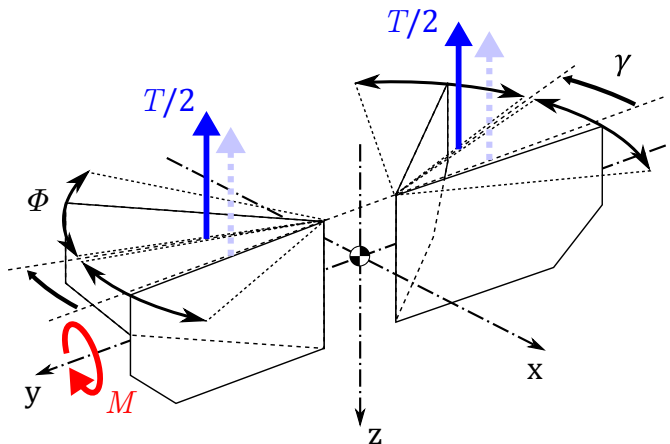


Figure 2: Pitch moment generation mechanism of the *DelFly Nimble*: moving the flapping wings back by a dihedral angle  $\gamma$  shifts the mean thrust  $T$  backwards and results in a nose-down moment  $M$ .

*DelFly Nimble* has no tail; instead, the robot is stabilized and controlled only through its wing actuation system. The robot has two separate flapping mechanisms, each driving its own wing pair on the left and right side. The independent modulation of flapping frequency, and thereby thrust, on each side allows for roll control. A servo-driven gear mechanism between the two flapping mechanisms allows to change the dihedral angle, i.e. the angle between the wing-closed positions, which results in a longitudinal shift of the flap averaged thrust forces and provides pitch control (see Figure 2). The bottom servo offers yaw control by deflecting the wing surfaces such as to tilt the thrust vectors of the two wing pairs in opposite directions.

Unlike in [32], the robot used here is equipped with a lighter, yet more powerful, 1.5 g Lisa MXS autopilot [34]. A micro SD card was used for storing on-board data logs. Four custom made reflective markers (10 mm styrofoam balls covered in reflective tape) were attached to the robot such that it could be tracked with a motion capture system. The details on the robot’s control system as well as its performance can be found

in [32].

The flights were recorded in two ways. On-board Euler angle estimates, gyro readings, radio control set points, on-board generated controller references, controller outputs, and motor speeds were recorded onto the micro SD card at a rate of approximately 100 Hz. At the same time, the position and orientation of the robot was recorded with an OptiTrack motion tracking system. Most flights were performed in the Cyberzoo facility of Delft University of Technology, which is a 10 m × 10 m × 7 m flight arena equipped with 12 OptiTrack Prime 17W cameras. The position and orientation data was captured at 200 Hz. Since this setup did not provide enough space for high speed tests, these were performed in a large indoor flight hall with 12 Flex13 cameras covering a tracking volume of approximately 8 m in length and 4 m in width and height on one side of the hall. This setup allowed to approach the robot's maximal speed prior to entering the tracking volume. These tests were recorded at a rate of 120 Hz. Videos from some of the flight tests are available online: [https://www.youtube.com/playlist?list=PL\\_KSX9G0n2P8nD6go-RTL9Vp\\_Mb08b5jn](https://www.youtube.com/playlist?list=PL_KSX9G0n2P8nD6go-RTL9Vp_Mb08b5jn).

The velocities and accelerations were obtained from the motion tracking data by time differentiation using a central difference scheme such that no phase lag was introduced. In [35] this technique was successfully used to estimate the sub-flap forces acting on a FWMAV in flight, where the errors resulting from the numerical differentiation were also thoroughly analysed. The differentiated measurements were then filtered with a 4th order Butterworth filter with a 5Hz cut-off frequency such the noise due to measurement error, amplified by the differentiation, as well as due to flapping-induced body oscillations was attenuated.

The actuator dynamics were identified using the data from our previous test-bench experiments presented in [32], captured with a high precision force balance system (Nano17-Ti, ATI Industrial Automation, Inc.) and a high-speed data acquisition system (NI cRIO-9024 FPGA, National Instruments). The wind tunnel used to collect data about trimmed flight was the Open Jet Facility (OJF) of Delft University of Technology.

### 3 LONGITUDINAL DYNAMICS MODEL

Here we present a longitudinal dynamics model of a tailless flapping wing robot, which is based on the linear damping model [30, 31], and which is applicable to flight conditions ranging from hovering to forward cruise flight. Compared to previous models of the same type, e.g. [9], we include also the vertical dynamics (necessary for non-hovering flight) and the pitch control mechanism. Experimental data is used to identify the model parameters, and finally to validate the model. The overall model structure, which was implemented in Simulink (MATLAB 2016b, Mathworks, Inc.) is shown in Figure 3. This section will focus on its open loop part.

#### 3.1 Linear drag model

The validity of approximating the body-motion-induced flap-average drag force of flapping wings with a linear damping force was demonstrated e.g. in [3], employing the quasi-steady assumption [36]. Assuming a model case, where a wing flaps with constant velocity and angle of attack in both upstroke and downstroke (saw tooth flapping profile), the wing velocity at the centre of pressure (assumed to lie at half of the wing length  $R$  for simplicity) can be written as  $U = 2\Phi f \frac{R}{2} = \Phi f R$ , where  $\Phi$  is the flapping amplitude and  $f$  the flapping frequency. If  $u$  is the body velocity (which can also be considered as the free stream velocity), the wing airspeed will then be  $U_a = U + u$  during downstroke and  $U_a = U - u$  during upstroke (Figure 4). We express the drag force, which acts opposite to  $U_a$ , in the form  $d = \hat{b}U_a^2$ , where  $\hat{b}$  is a force coefficient, which in our case is constant (the angle of attack is assumed to be constant). The drag force during the upstroke and downstroke (defined as positive when in the direction of body motion  $u$ ) is  $d_d = -\hat{b}(U + u)^2$  and  $d_u = \hat{b}(U - u)^2$ , respectively. Since the two strokes have an equal time duration, the average force over a flapping cycle reduces to  $\bar{d} = \frac{1}{2}(d_d + d_u) = \frac{1}{2}\hat{b}[-(U + u)^2 + (U - u)^2]$ , which can be reduced to  $\bar{d} = -2\hat{b}Uu$ , i.e. the drag force is a linear function of the body velocity  $u$ . However, this is only true if  $u < U$ . If  $u > U$ , the drag force will always point in the direction opposite to the body motion  $u$ , irrespective of the flapping motion direction. The drag in the downstroke will be  $d_u = -\hat{b}(U - u)^2$ , and the flap-averaged force will remain nonlinear with respect to  $u$ ,  $\bar{d} = \frac{1}{2}\hat{b}[-(U + u)^2 - (U - u)^2] = -\hat{b}[U^2 + u^2]$ . Figure 5 compares the velocity component of the cycle-averaged drag force with and without the simplifying assumption  $u \ll U$ . When the ratio of the body velocity to wing velocity due to flapping  $u/U$  is higher than 1, the non-linearity of the drag force becomes apparent. At  $u/U = 2$ , which we consider to be the limit of validity of our model, the error between the linear and non-linear model is about 20%, which we consider still acceptable for stability analysis and control design purposes. Since wing length  $R$  and flapping amplitude  $\Phi$  are constant, we can rewrite the drag force as

$$\bar{d} = -2\Phi R f \hat{b} u = -b f u, \quad (1)$$

where  $b$  is a force coefficient depending on the wing geometry and kinematics, but independent of flapping frequency.

Linear damping models have been shown to predict well the horizontal drag forces of flapping wings measured in a wind tunnel [3]. Moreover, the linear damping character of the drag forces in all the body directions, termed flapping counter force, was demonstrated analytically using a quasi-steady model in [14], which justifies its use also for the drag force in the vertical body direction.

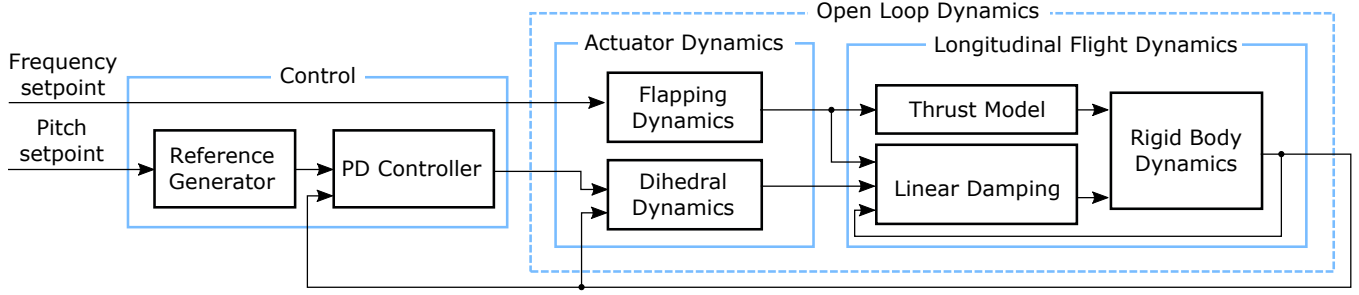


Figure 3: Overall model structure.

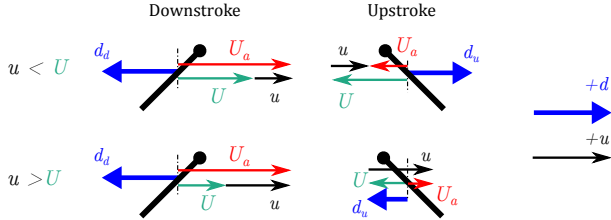


Figure 4: Linear drag model: drag force direction in downstroke (drag  $d_d$ ) and upstroke ( $d_u$ ) for  $u < U$  (top row) and for  $u > U$  (bottom row).

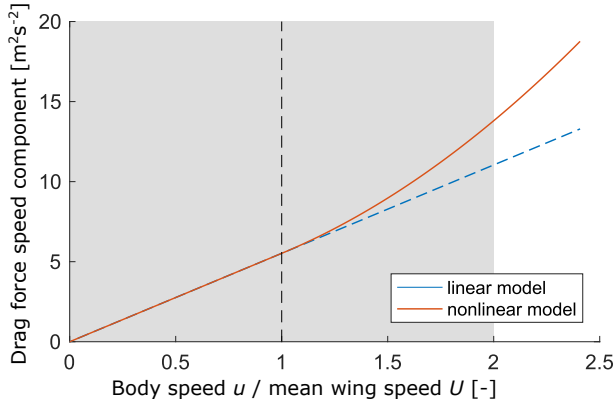


Figure 5: The validity region of the linear drag model. Comparison of a linear and nonlinear drag force models ( $f = 17$  Hz,  $\Phi = 40^\circ$ ,  $R = 0.14$  m, resulting in  $U \approx 1.7$  m/s). The non-linearity becomes apparent for  $u/U > 1$ , the grey shading shows the considered validity region (max. error  $\approx 20\%$ ).

### 3.2 Flight dynamics

The robot is considered to be rigid and its movable parts (including the wings and the flapping mechanisms) massless. This means that the center of mass (CoM) is a fixed location within the flapper body. The standard rigid body equations of motion can be used in this case [37]. In this study, we constrain ourselves to the longitudinal dynamics, assuming a perfect symmetry of the robot and no wind, i.e. wind speed is

equal to air speed:

$$m\dot{u} = -m\dot{\theta}w - mg \sin \theta + X \quad (2)$$

$$m\dot{w} = m\dot{\theta}u + mg \cos \theta + Z \quad (3)$$

$$I\ddot{\theta} = M. \quad (4)$$

Here  $m$  is mass,  $I$  moment of inertia along the lateral body axis,  $g$  gravitational acceleration,  $u$  longitudinal body velocity,  $w$  vertical body velocity,  $\theta$  body pitch angle,  $X$  longitudinal body force,  $Z$  vertical body force and  $M$  the pitch torque. The equations of motion follow the standard aerospace notation, where the forces, moments and velocities are expressed in body-fixed coordinates.

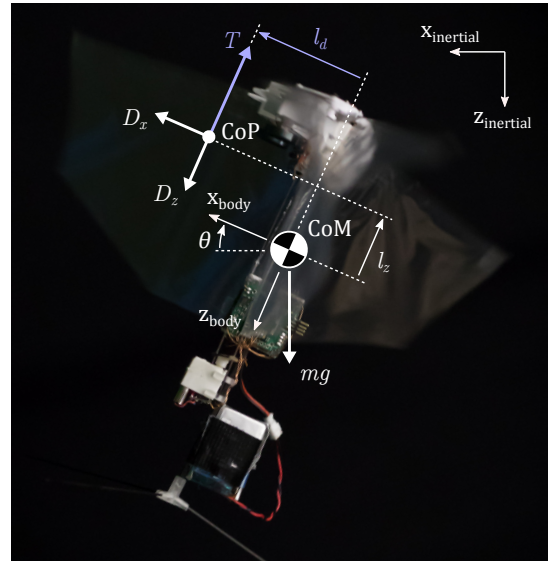


Figure 6: 2D longitudinal free body diagram of a flapping-wing MAV (side view). CoP represents the mean center of pressure, CoM the center of mass. Blue color indicates the control variables.

The free body diagram of the robot's model is shown in Figure 6. All the aerodynamic effects originate from the flapping wings, the drag of the body is neglected. The two wing pairs

are represented by a thrust force  $T$  and a drag force  $D$ , both acting at the flap-averaged center of pressure (CoP). The adjustable dihedral angle of the real robot, used for pitch torque generation, is represented in the model by the adjustable longitudinal position  $l_d$  of the CoP with respect to the CoM. Because the model should be applicable to flight in any direction, the drag force  $D$  has longitudinal and vertical components

$$D_x = -b_x f u_{CoP} \quad (5)$$

$$D_z = -b_z f w_{CoP}, \quad (6)$$

where  $b_x$  and  $b_z$  are the force coefficients in the respective axes, capturing the drag effects of both wing pairs, and  $u_{CoP}$  and  $w_{CoP}$  are the longitudinal and vertical components of the CoP velocity. The CoP velocities can be expressed as

$$u_{CoP} = u - l_z \dot{\theta} + \dot{l}_d \quad (7)$$

$$w_{CoP} = w - l_d \dot{\theta}, \quad (8)$$

where  $l_d$  and  $l_z$  represent the longitudinal (adjustable) and vertical (fixed) CoP location in the body frame, respectively. Because  $l_d$  changes over time as it is used for pitch control, its time derivative  $\dot{l}_d$  is also included in the velocity expressions; the corresponding term had a non-negligible effect on the results of closed loop simulations.

The thrust force  $T$  generally depends on the flapping frequency  $f$ . To keep the model applicable to a general vehicle, we will assume a general function  $T(f)$ . The function applicable to the vehicle used for model validation will be identified in the next section.

Following the free body diagram in Figure 6 and combining (5-8), the body forces and moment are found as

$$X = D_x = -b_x f (u - l_z \dot{\theta} + \dot{l}_d) \quad (9)$$

$$Z = D_z - T = -b_z f (w - l_d \dot{\theta}) - T(f) \quad (10)$$

$$\begin{aligned} M &= D_x l_z + (D_z - T) l_d = \\ &= -b_x f l_z (u - l_z \dot{\theta} + \dot{l}_d) + b_z f l_d (w - l_d \dot{\theta}) - T(f) l_d. \end{aligned} \quad (11)$$

Finally, inserting equations (9-11) into (2-4) yields the complete set of longitudinal flight dynamics equations

$$m\dot{u} = -m\dot{\theta}w - mg \sin \theta - b_x f (u - l_z \dot{\theta} + \dot{l}_d) \quad (12)$$

$$m\dot{w} = m\dot{\theta}u + mg \cos \theta - T(f) - b_z f (w - l_d \dot{\theta}) \quad (13)$$

$$I\ddot{\theta} = -b_x f l_z (u - l_z \dot{\theta} + \dot{l}_d) + b_z f l_d (w - l_d \dot{\theta}) - T(f) l_d. \quad (14)$$

The model has 2 inputs (the adjustable horizontal CoP location  $l_d$  and the flapping frequency  $f$ ) and only 5 parameters (mass  $m$ , moment of inertia  $I$ , drag force coefficients  $b_x$  and  $b_z$ , and vertical location of the CoP  $l_z$ ). We will discuss the parameter identification in Section 3.5.

### 3.3 Thrust model

Making the assumption that the produced thrust only depends on the flapping frequency and is insensitive to the body air speed (these effects will be partially modeled by the linear damping), the thrust to flapping frequency relationship can be found experimentally in still air using a force balance. The thrust force  $T$  has been found to depend on the second power of flapping frequency  $f$  in a hummingbird-like flapping wing robot [38]. However, the DelFly designs with X-wing configuration exploit the clap-and-peel thrust-enhancing mechanism [33], and the thrust to flapping frequency relationship can be approximated by a linear function in the neighborhood of operational flapping frequencies. This is also the case for the DelFly Nimble (Figure 7) with an operating frequency  $\sim 17$  Hz in hover. Thus, a linear fit of this relationship from [32] was incorporated into the dynamic model as

$$T = 2(c_1 f + c_2), \quad (15)$$

where  $c_1$  and  $c_2$  are the fitted coefficients (see Table 2) and  $f$  is the flapping frequency. The factor of two accounts for having two wing pairs.

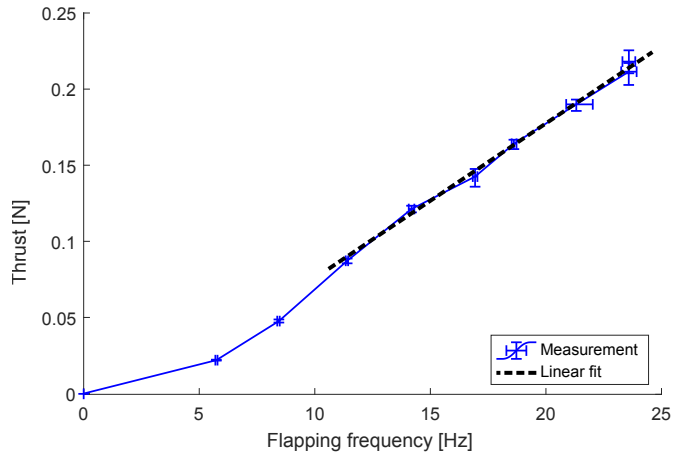


Figure 7: Thrust of a single wing pair versus flapping frequency. Each data point represents an average over a 2-s measurement, the error bars represent the standard deviation.

### 3.4 Actuator dynamics

Because the on-board actuators cannot reach infinite accelerations, their dynamics need to be included in the model. We have performed the experiments necessary for their identification in our previous work [32].

To determine the dihedral actuator dynamics, a pulse train was sent to the dihedral servo actuator while both wing pairs were flapping. Because we could not measure the dihedral angle with high accuracy, we used the pitch moment measurements during a tethered test on a force balance instead (flapping frequency approximately 14 Hz). The pitch moment, filtered with a low-pass fourth order Butterworth filter with

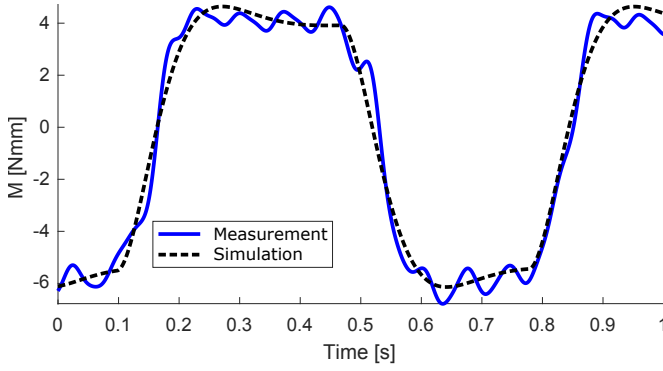


Figure 8: Measured and simulated (second order transfer function) pitch moment in response to a series of step commands. The minimum and maximum dihedral servo command was 28% and 68%, respectively, both flapping mechanisms were driven with a 50% throttle command, which resulted in a flapping frequency of approximately 14 Hz.

a cutoff frequency of 10 Hz to keep only the sub-flapping-frequency signals characterizing the actuator dynamics, is shown in Figure 8. Because of the observed response type, typical for a second order linear system, a second order transfer function was chosen

$$H_{dihed} = \frac{\omega_n^2}{s^2 + 2\xi\omega_n s + \omega_n^2}, \quad (16)$$

where  $\omega_n$  is the natural frequency and  $\xi$  the damping ratio. The transfer function parameters were estimated with the *tfest()* function from the Matlab 2016b System Identification toolbox. Figure 8 confirms that the second order system with the identified parameters ( $\omega_n = 24 \text{ rad}\cdot\text{s}^{-1}$ ,  $\xi = 0.634$ ) is a good approximation of the dihedral angle dynamics on a test bench. The identified natural frequency corresponds to approximately 3.8 Hz, which is well below the cutoff frequency of the low-pass filter. The actuator dynamics was thus well preserved in the filtered signal.

In flight, an additional effect was found to influence the dihedral angle of the wings. In forward flight maneuvers recorded during the trials described in [32], an error between the commanded and measured dihedral angle of the wings was observed, see Figure 9. This error, specific to the design of the robot's dihedral actuation mechanism, is likely due to mechanical elasticity or even play, but it could also be a steady state error of the controller of the dihedral servo in the presence of aerodynamic drag in forward flight. We have noticed that this error strongly correlates with the body axis velocity  $u$ . Figure 9 shows that an additional correction factor in the form  $c_{corr}u$  can predict this error reasonably well. The parameter  $c_u$  was found by numerical optimization (*lsqnonlin()* function of Matlab 2016b), see Table 2.

By including this term, the dihedral angle model becomes

$$\gamma = \gamma_{sim} + c_{corr}u, \quad (17)$$

where  $\gamma_{sim}$  is the dihedral angle estimated by the transfer function (16) and  $\gamma$  is the dihedral angle after corrections.

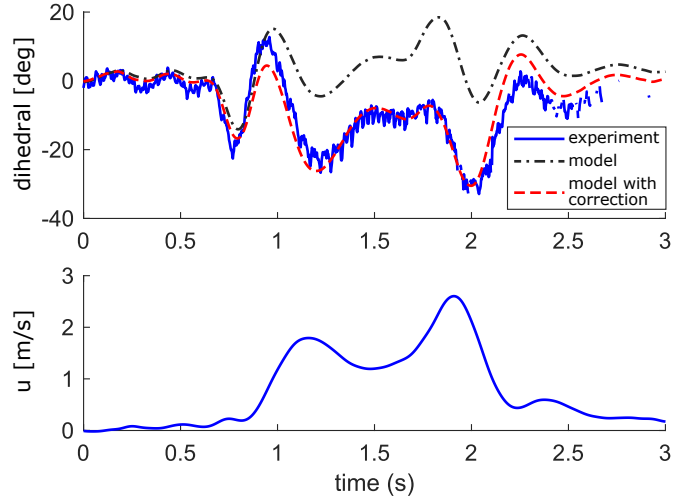


Figure 9: Measured and modeled dihedral angle. A correction proportional to forward velocity  $u$  was applied to compensate for the initial model error.

To convert the dihedral angle  $\gamma$  to the horizontal CoP position  $l_d$  we need the distance  $l_w$  from the dihedral mechanism hinge to the CoP of the wing pair on one side of the robot

$$l_d = l_w \sin \gamma. \quad (18)$$

We estimated  $l_w$  from the pitch moment measurements as  $l_w = \frac{M}{T \sin(\gamma)}$ , where  $T$  is the thrust average over the whole two second measurement,  $M$  is the steady state of the filtered pitch moment achieved at the end of each pulse, and  $\gamma$  is the dihedral angle at the end of each pulse, which we could measure in a static case, when the wings were still.

The actuator dynamics of the motor-driven flapping mechanism was determined from an experiment where a pre-programmed pulse train was sent to the motor controller and the flapping frequency was recorded. A first order transfer function in the form

$$H_{flap} = \frac{1}{\tau s + 1} \quad (19)$$

was again estimated with the *tfest()* function from the Matlab 2016b System Identification toolbox on the basis of the unfiltered flapping frequency measurements and the commands.  $\tau$  is the first order system time constant, its identified value is in Table 2. A response simulated with the estimated transfer function in Figure 10 demonstrates that the first order system is a good representation of the flapping mechanism dynamics.

### 3.5 Model parameters identification

The flight dynamics equations (12-14) contain only 5 parameters that need to be identified: mass  $m$ , force coefficients  $b_x$

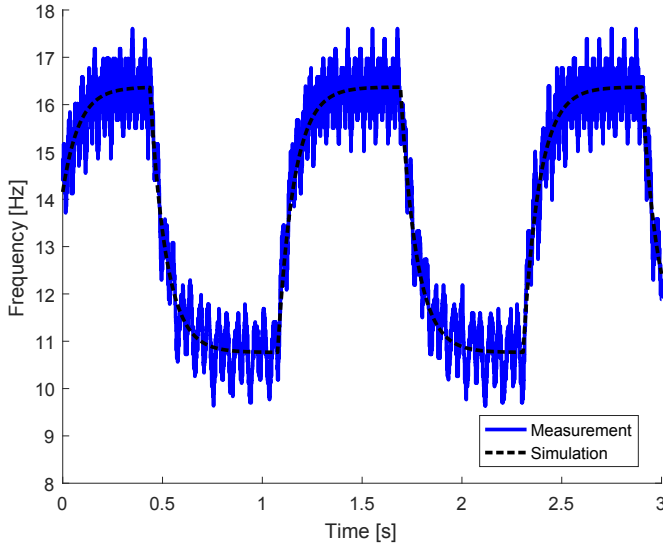


Figure 10: Measured and simulated (identified first order transfer function) flapping frequency in response to a series of step commands. The motor speed controller command consisted of a pulse train with a minimum and maximum throttle value of 36.7% and 53%, respectively.

and  $b_z$ , moment of inertia  $I$ , and vertical location of the CoP  $l_z$ .

The mass of the robot prototype was measured by a precision scale (Adam Equipment PGW 4502e). The moment of inertia was estimated from the locations and masses of its individual components. Alternatively, it can be estimated from an (accurate) CAD model or experimentally, e.g. using a bifilar vertical-axis torsional pendulum method [39].

Since our robot was flight capable and stable at a wide range of flight speeds (thanks to its active on-board stabilization [32]), we estimated the force coefficients from trimmed steady level flights at various wind speeds, performed in a wind tunnel. Alternatively, a static wind-tunnel experiment, such as in [3], or a pendulum test, such as in [40], can also be used to estimate the force coefficients.

When collecting the flight data, a human pilot flew the robot in the test section of an open jet wind tunnel (Open Jet Facility at Delft University of Technology, test section 2.8 m  $\times$  2.8 m) at various wind speeds between 1 - 2.4 m/s. The velocity reading of the wind tunnel is not reliable below this range and above that it becomes difficult for the pilot to keep the robot in steady flight in the center of the open jet test section. The data logged on-board included the flapping frequency and the body pitch angle, and the wind speed was logged simultaneously off board.

Assuming steady state in the translation equations (12-13), the accelerations  $\dot{u}$  and  $\dot{w}$ , angular rate  $\dot{\theta}$  as well as derivative of the (adjustable) horizontal CoP location  $\dot{l}_d$  are zero and the

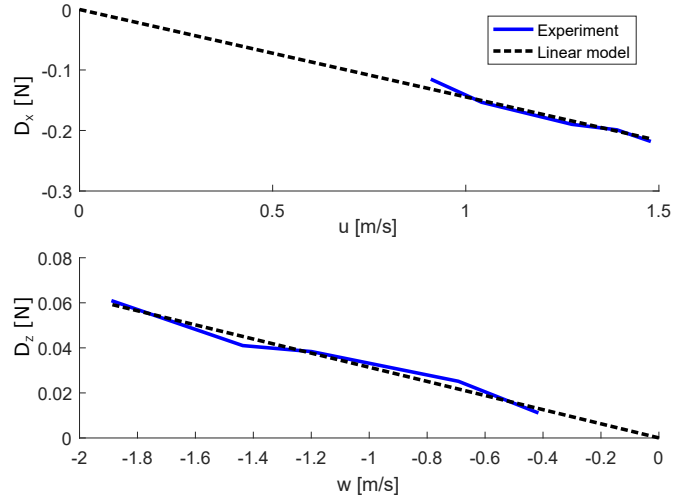


Figure 11: Drag forces estimated at steady level flight at various wind speeds and a linear model fit. The maximal  $u$  and  $w$  during this test correspond to  $u/U \approx 0.9$  and  $w/U \approx 1.1$ .

aerodynamic drag forces can be expressed as

$$D_x = -b_x f u = mg \sin \theta \quad (20)$$

$$D_z = -b_z f w = -mg \cos \theta - T. \quad (21)$$

For each wind tunnel speed set point, we estimated the steady state conditions by averaging the data over a several second long segment where the pilot managed to keep the robot in near-steady flight. The body velocity components  $u$  and  $w$  were computed from the averaged body pitch and wind speed. The generated thrust was estimated from the averaged flapping frequency  $f$  using the relationship 15. In total 5 trim points yielded an overconstrained system of equations that was solved for  $b_x$  and  $b_z$  using the linear least squares method. A comparison of the obtained linear model and the drag forces estimated at each condition is shown in Figure 11, confirming that the linear model is a good approximation.

The last unknown parameter is the vertical CoP location  $l_z$ . For the initial estimate, we adopted the common assumption of simpler quasi-steady models that the CoP lies at a quarter-chord distance from the wing leading edge.

### 3.6 Open loop validation

To validate the open loop model, we have used existing flight data recorded during the experiments described in [32]. Namely, we have selected 3 maneuvers: a maneuver where the vehicle quickly transitions from hover to forward flight and returns back to hover and a maneuver where the vehicle starts a vertical climb and returns back to hover, and finally a 360-deg pitch flip maneuver. The motion tracking and on-board logged data contained the vehicle states needed to estimate the dihedral angle  $\gamma$  and to evaluate the state derivatives according to equations (12-14). In these experiments the flapping frequency  $f$  was measured only on the right wing

(limitation of the autopilot board), but a perfect symmetry was assumed. The estimates were compared to the filtered state derivatives (4th order Butterworth filter, 5Hz cut off) that were derived directly from the flight data. The 5Hz cutoff frequency was chosen to suppress the (high frequency) oscillations due to flapping, but keep the (low frequency) body dynamics.

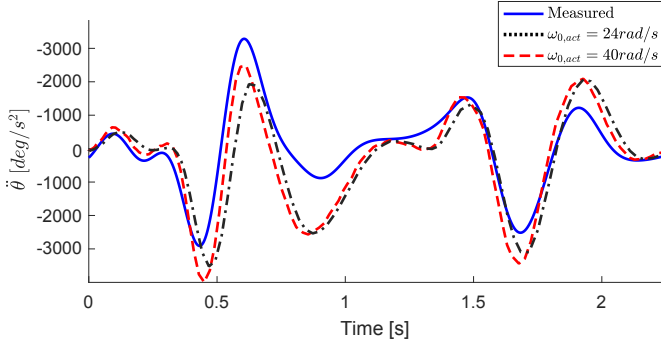


Figure 12: Pitch acceleration measured in flight and predicted by the model. The natural frequency of the dihedral actuator model was adjusted to achieve a better phase match.

The initial results revealed that the identified model of the dihedral actuation mechanism underestimated its bandwidth. Figure 12 compares the estimated and measured pitch acceleration. While in general the two curves match reasonably well, the estimated acceleration peaks lagged behind the measurements. We have thus increased the natural frequency of the actuator to almost twice the original value (from 24 to 40 rad/s) to improve the phase match. We hypothesize that our originally identified natural frequency was too low because, unlike in flight, the vehicle body was clamped during the force balance tests. It is likely that in free air, due to action and reaction principle, the body moves opposite to the wings when the dihedral angle is being adjusted, and thus the work done by the dihedral actuator is lower than when the body is fixed.

In Figure 13, the state derivatives predicted by the model (with the optimized actuator dynamics) are compared to the filtered measurements for a pitch maneuver. Despite minor differences, qualitatively speaking, all state derivatives and even the dihedral angle follow their expected trends well. This is also confirmed by the correlation coefficients ( $\dot{u}$ : 0.91,  $\dot{w}$ : 0.98,  $\dot{q}$ : 0.86,  $\gamma$ : 0.89) and low range-normalized root-mean-square error (NRMSE) values ( $\dot{u}$ : 0.082,  $\dot{w}$ : 0.048,  $\dot{q}$ : 0.116,  $\gamma$ : 0.095).

Figure 14 shows the model predictions and filtered measurements for a vertical climb maneuver. Again a good overall match can be seen. The vertical acceleration  $\dot{w}$  seems to be predicted less well around  $t = 3$  s, when the flapping frequency returns back to the value ensuring trimmed hovering flight. Possibly, additional non-linear effects (not covered by our model) are present in this phase, where the vehicle still

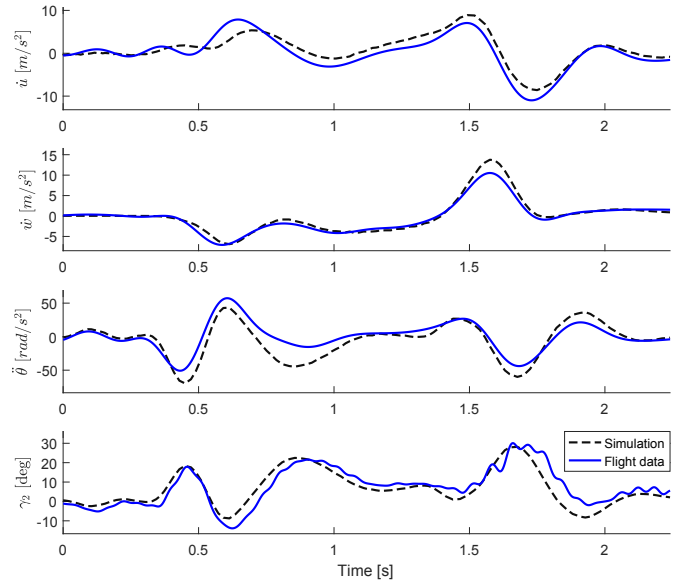


Figure 13: Pitch maneuver: measurement vs open loop model prediction of the state derivatives and hinge angle.

moves upwards at a considerable speed while the flapping frequency is decreasing. Nevertheless, the good overall match is also illustrated by high values of correlations coefficients ( $\dot{u}$ : 0.79,  $\dot{w}$ : 0.98,  $\dot{q}$ : 0.83,  $f$ : 0.95) and low NRMSE ( $\dot{u}$ : 0.145,  $\dot{w}$ : 0.067,  $\dot{q}$ : 0.125,  $f$ : 0.091), especially for the excited degrees of freedom  $\dot{w}$  and  $f$ .

Finally, Figure 15 shows the results for a 360-degree pitch flip. This maneuver consists of several phases: 1) a vertical climb to gain altitude, 2) a pitch acceleration by commanding maximal dihedral deflection  $\gamma_{cmd}$  (effectively a response to an open loop step command), 3) a free rotation where neutral dihedral angle and minimal flapping frequency are commanded, and finally 4) return to the closed loop stabilization once the pitch rotation, monitored by integrating the pitch rate, approaches 270 degrees. Due to flat tracking markers placed on the flapping mechanisms, the motion-tracking-based dihedral angle measurement is only available for a limited range of pitch angles around the vertical (hovering) body orientation [32]. Even such an extreme and highly nonlinear maneuver is predicted fairly well by the model, as confirmed by the correlation coefficient values ( $\dot{u}$ : 0.91,  $\dot{w}$ : 0.86,  $\dot{q}$ : 0.90,  $\gamma$ : 0.73,  $f$ : 0.93) and NRSME values ( $\dot{u}$ : 0.061,  $\dot{w}$ : 0.169,  $\dot{q}$ : 0.058,  $\gamma$ : 0.15,  $f$ : 0.074).

Because our aim is to develop a complete closed loop model, more detailed validation is given in the next section that also includes the controller. Since the flapping frequency is controlled manually by the pilot through the throttle stick, and (unless climbing or performing fast forward flight) the adjustments in typical flight conditions are only marginal (ensuring trim of the vehicle), we will further focus only on the pitch maneuvers that require auto-stabilization of the pitch rotation.

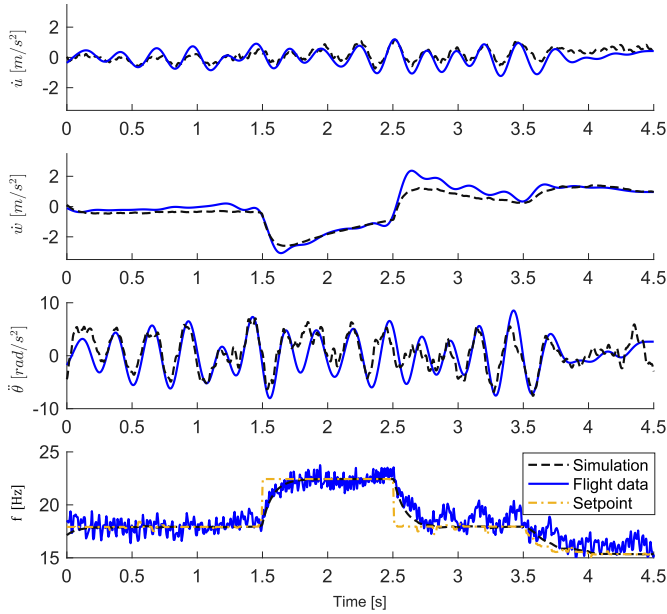


Figure 14: Climb maneuver: measurement vs open loop model prediction of the state derivatives and flapping frequency (right wing pair).

#### 4 CLOSED LOOP MODEL AND ITS VALIDATION

Because tailless flapping flight is inherently unstable [12, 11, 41, 10, 22], active stabilization is necessary to keep the balance and stay aloft. It is hypothesized that natural flyers primarily rely on proportional feedback on body rates [31, 42, 43], and similar control systems are used in man-made tailless systems [5, 7, 8, 9], including the DelFly Nimble [32]. In this section, we extend the model with the control system used on-board of the robot. We describe the experiments carried out to collect data for fine tuning of the closed loop model parameters. We report on experiments used for the final model validation, which included a change of the center of gravity, moment of inertia and a change of the control parameters. Finally, results of the validation are presented.

##### 4.1 Controller

The DelFly Nimble is being stabilized by a fixed-gain parallel feedback architecture, which involves rate and attitude feedback [32]. The controller layout, reduced to the longitudinal case, is shown in Figure 16. This is the standard controller architecture in the open-source Paparazzi UAV autopilot software (version 5.12), with the addition of the low-pass filter on the commands. The reference attitude and rate are generated from the attitude setpoint given by the pilot (received via RC) via a second order system reference generator, described in [32]. Its function will be demonstrated in Section 4.3, Figure 18.

Despite a vibration isolator, which is used to mount the autopilot to the robot’s fuselage [32], some of the high fre-

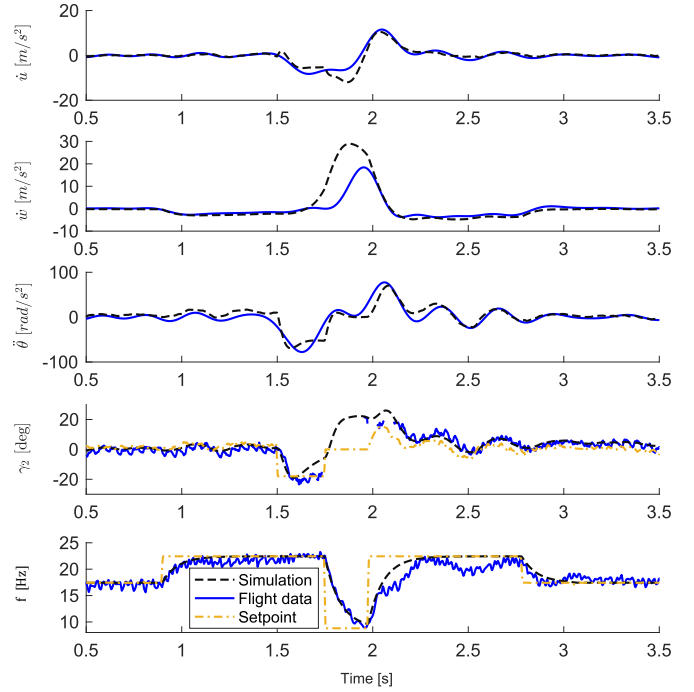


Figure 15: 360-degree pitch flip maneuver: measurement vs open loop model prediction of the state derivatives, dihedral angle and flapping frequency (right wing pair).

quency mechanical vibration of the fuselage (excited by the flapping wings) is captured by the on-board sensors and propagates through the feedback control loop. The final command is thus filtered by a second order Butterworth filter (biquad implementation,  $f_{cut} = 15$  Hz cut-off frequency) before being sent to the actuators in order to reduce the high frequency signal ”noise”. The controller parameters, identical in our simulations as well as in the test flights, were  $K_P = 0.511$  and  $K_D = 0.0654$  s.

##### 4.2 Model parameter optimization

To achieve the best match between the simulation and recorded flight data, we have optimized the flight dynamics parameters that were only roughly approximated in the initial

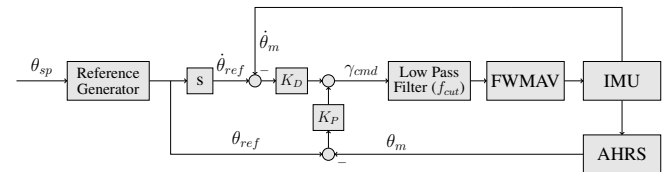


Figure 16: Controller architecture, where set point is denoted by subscript  $sp$ , reference by subscript  $ref$  and measurement by subscript  $m$ . The parameters used in the simulations as well as in the test flights were  $K_P = 0.511$ ,  $K_D = 0.0654$  s and  $f_{cut} = 15$  Hz.

open loop validation, namely the CoP vertical location  $l_z$  and the moment of inertia  $I$ . Because of the minimalist nature of the flight dynamics model, estimating these parameters from free-flight data was desirable as the optimized values could also capture, to some extent, the unmodeled phenomena, such as added mass inertia.

The flight data collected for the optimization purposes consisted of a set of remotely-piloted pitch maneuvers, where the pilot commanded various set points (ramps and steps of various magnitudes and durations, see Figure 17), such that a significant part of the longitudinal system flight envelope was covered. These maneuvers were different to the ones used in the validation phase, such that the validation could detect possible overfitting of the model. Since  $l_z$  and  $I$  mainly influence the pitch attitude dynamics, the cost function to be minimized was simply the sum of squares of the errors between the simulated and the recorded pitch angle. In this way we could avoid a multi-objective optimization that would be necessary if also the velocity states were included. A particle swarm global optimization routine [44] was used to minimize the cost function. The optimized parameter values are listed in Table 2.

The optimized  $l_z$  and  $I$  values show that our initial estimates used in the OL simulations might have been imprecise, however, it is also possible that the optimization results account for some of the unmodified phenomena. Finally, unlike the flight data used in the OL simulations, the flight data used in the CL optimization was recorded with a different vehicle, equipped with a new, lighter autopilot board, which can also explain some of the differences.

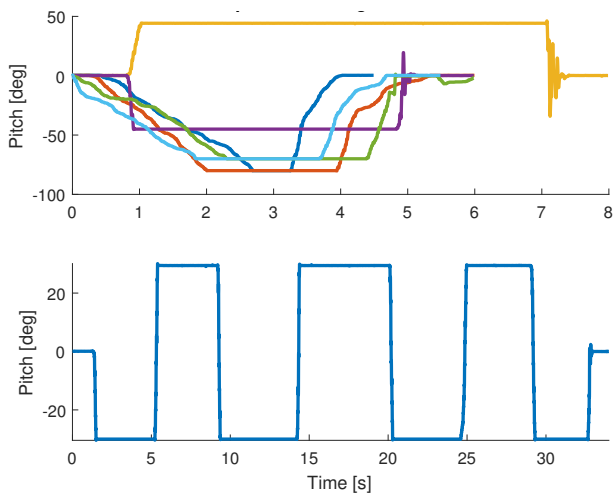


Figure 17: Model fitting maneuver set points, shown in two separate plots due to different time scales.

### 4.3 Validation procedure

When collecting the flight data for model validation, we had three goals in mind. First, we wanted to verify that the model

is valid for flight conditions ranging from hover to fast forward flight. Second, we wanted to test whether physical changes to the robot, such as a change of the CoM and moment of inertia, will be captured correctly by the model. Finally, we wanted to test whether changes to the control system parameters have the same effect in simulation as well as in real flight.

The flights of all data sets included step-like pitch commands, starting at a near-hover condition, i.e. with zero attitude set point and a throttle set point that resulted in zero vertical acceleration. The commands were given manually to maintain control of the robot at all times in order to avoid flying into the sides of the motion tracking arena. However, repeatability of individual trials was ensured by: 1) the reference generator, which "filtered" the pilot's manual step-like commands (set points  $\theta_{sp}(t)$ ) into nearly identical attitude reference time histories  $\theta_{ref}(t)$  (see Figure 18) and 2) by pre-programming the maximal pitch set point value  $\theta_{spmax}$ . The maneuvers were aligned in time at the point where their pitch references  $\theta_{ref}$  reached  $10^\circ$ .

For each test condition, the maneuver was repeated at least five times. Each recorded trial was simulated using the onboard-recorded pitch set point as model input. Because the thrust produced at a constant throttle setting varies with the battery voltage (a phenomena not captured by our model), a flapping frequency resulting into thrust force that is equal to the vehicle weight (inverse of (15)) was used in the simulations instead. The mean and the standard deviation was calculated for the measured and simulated states of each maneuver.

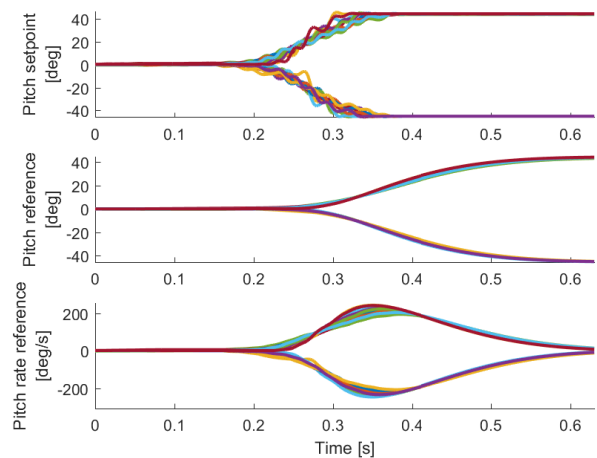


Figure 18: Comparison of 45 degree pitching maneuver set points and references.

### 4.4 Validation results

In the first validation set (Figure 19), we compare the simulated and recorded response for pitch step commands of  $15^\circ$ ,  $30^\circ$ ,  $45^\circ$  and  $60^\circ$ . The solid lines represent the average mea-

Table 2: Model parameters used in open loop (OL, Section 3.6) and closed loop (CL, Section 4.4) simulations.

Parameter	Value		Unit	Source
	OL	CL		
$m$	29.4		$g$	Measured
$I_{yy}$	1.00e-4	1.26e-4	$kgm^2$	Flight data (Section 4.2)
$b_x$	4.21e-3		$Ns^2m^{-1}$	Wind-tunnel-flight data (Section 3.5)
$b_z$	9.16e-4		$Ns^2m^{-1}$	Wind-tunnel-flight data (Section 3.5)
$l_w$	81		$mm$	Force balance data (Section 3.4)
$l_z$	11.0	27.1	$mm$	Flight data (Section 4.2)
$\omega_n$	40		$s^{-1}$	Flight data, tuned manually (Section 3.6)
$\zeta$	0.634		—	Force balance data (Section 3.4)
$c_{corr}$	0.175		$sm^{-1}$	Flight data (Section 3.4)
$\tau$	0.0796		$s$	Force balance data (Section 3.4)
$c_1$	0.0114		$NHz^{-1}$	Force balance data (Section 3.4)
$c_2$	-0.0449		$N$	Force balance data (Section 3.4)

sured state and the dashed lines the average simulated state. The shaded regions represent the standard deviation. It can be appreciated, that the experiments are highly repeatable. In general, the simulation is in a very good agreement with the experimental results. The damping of the real system seems to be slightly weaker than in simulation, the oscillations are attenuated earlier in the model. The horizontal body speed component  $u$  is predicted less well by the model, which also under-predicts its steady state value, but the trends remain well captured.

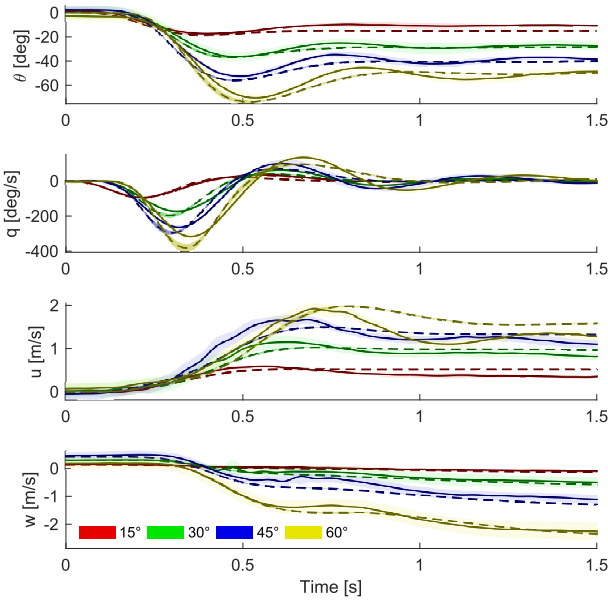


Figure 19: Comparison of forward pitching maneuvers in balanced configuration for various pitch set point values (color coded according to the legend). Solid lines correspond to mean measured states, dashed lines to mean simulated states. Belts around lines correspond to standard deviation.

The second set consists of 30° pitch step maneuvers performed with three different robot configurations. In the nominal, balanced configuration the CoM and CoP were aligned in longitudinal direction, i.e. the robot was trimmed to hover. In the “front heavy” configuration the battery was shifted forward, which resulted in an approximately 4.8 mm shift of the CoM towards the nose. Finally, in the “bottom heavy” configuration the battery was shifted down along the fuselage and the CoM was approximately 6 mm lower than in the balanced configuration. The change of moment of inertia due to the battery shift was estimated using the Steiner’s theorem.

A comparison of the recorded and simulated maneuvers for all three configurations is in Figures 20. The simulation results are again following the trends observed in the real flight data. As expected when using a controller without an integrator, a notable steady state error is present in the nose heavy configuration, where the vehicle is pitched slightly forward (and as a result flies forward) even with a zero attitude command. Similar positive bias in the pitch angle is observed after the step, compared to the balanced configuration, both in the simulated as well in the recorded flight data. The bottom heavy configuration, on the other hand, has trouble to reach the 30° reference, which is again expected, since the controller is competing against a stronger stabilizing aerodynamic moment due to forward flight. As in the first validation set, the higher order oscillations are attenuated faster in the simulation, and the  $u$  velocity is in general over predicted.

In the final data set, we performed 30° pitch-step maneuvers while varying attitude and rate feedback gains. A comparison of flight data and simulation results with different attitude feedback gains (while rate feedback gains were fixed) is given in Figure 21. The model correctly predicts the behaviour observed in flight, i.e. longer response times and over-damped response character for lower gains (green) and more apparent higher order oscillation for larger gains (blue), compared to the nominal case (red).

Figure 22 shows a comparison of captured and simulated

Table 3: Measurement versus simulations: correlation coefficients and range-normalized root mean squared errors (NRMSE)

Experiment	Correlation coefficient (-)				NRMSE				
	$u$	$w$	$q$	$\theta$	$u$	$w$	$q$	$\theta$	
Nominal (Step 30 deg)	0.98	0.89	0.96	0.98	0.066	0.145	0.026	0.050	Fig. 19-22
Step 15 deg	0.97	0.70	0.88	0.97	0.114	0.155	0.034	0.076	Fig. 19
Step 45 deg	0.98	0.97	0.96	0.99	0.054	0.115	0.028	0.032	
Step 60 deg	0.97	0.93	0.95	0.98	0.073	0.105	0.044	0.040	
Front heavy	0.99	0.82	0.95	0.99	0.073	0.149	0.025	0.035	Fig. 20
Bottom heavy	0.98	0.87	0.93	0.99	0.070	0.143	0.033	0.038	
Lower P gain	0.93	0.94	0.96	0.96	0.220	0.141	0.042	0.214	Fig. 21
Higher P gain	0.96	0.96	0.97	0.98	0.076	0.091	0.033	0.053	
Lower D gain	0.95	0.95	0.97	0.98	0.100	0.082	0.032	0.100	Fig. 22
Even lower D gain	0.96	0.97	0.97	0.98	0.107	0.099	0.040	0.086	

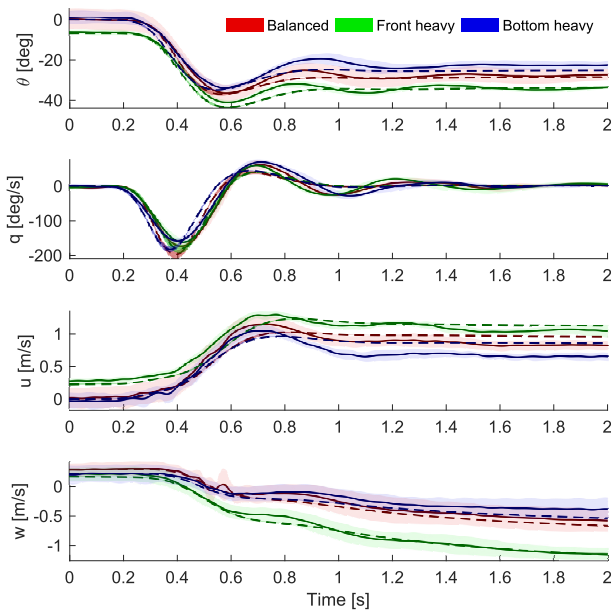


Figure 20: Averaged 30-degree forward pitching maneuvers in balanced/nose heavy/bottom heavy configurations (color coded according to the legend). Solid lines correspond to mean measured states, dashed lines to mean simulated states. Belts around lines correspond to standard deviation.

flights performed with different rate feedback gain values. Again, a good agreement is found between the experiment and simulation, both confirming that lowering the rate gains results in a less damped response and vice-versa.

#### 4.5 Analysis of model performance

The overall results demonstrate that the model, despite its simplicity, is able to capture the dominant dynamic effects well and that the simulated states were in a good agreement with the measurements. The good match is demonstrated also by high values of correlation coefficients and low range-normalized root mean squared errors, presented in Table 3 for

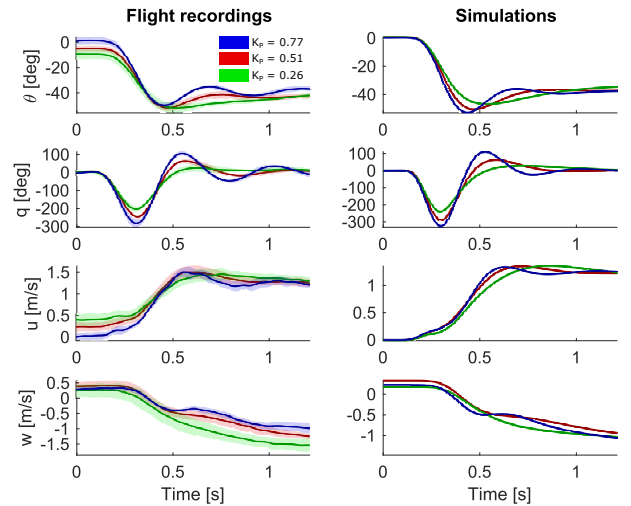


Figure 21: Comparison of flights with different attitude feedback gains (color coded), identical for the experiment and simulation. Solid lines correspond to mean states. Color belts around lines correspond to standard deviation.

all the validation sets.

The small differences observed can be attributed to unmodeled dynamics (unsteady aerodynamic effects, added mass inertia, hysteresis in the robot's pitch mechanism, ...), random external disturbances (light air drafts during the tests) as well as limitations of the measurement techniques (motion tracking and attitude estimation precision). One particular source of a slight disagreement between the recorded and simulated data could be the difference observed between the attitude estimated on board (used for control of the real vehicle) and the attitude estimated by the motion tracking system (used in the simulations). This time-dependent difference, combining the effects of estimation errors of both systems and imperfect alignment of their reference frames, always remained below 5 degrees. We preferred to use the motion-tracking-based at-

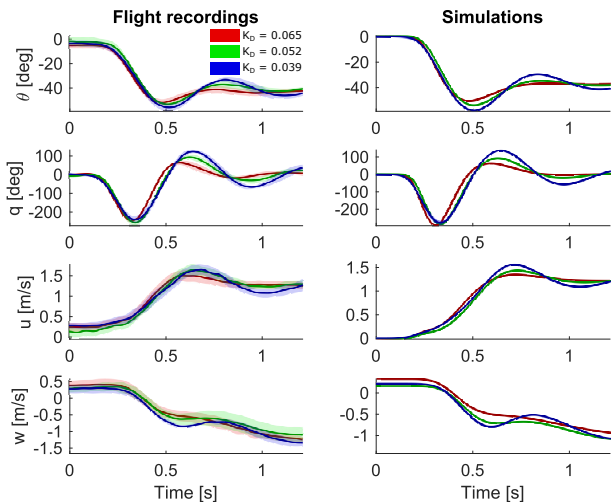


Figure 22: Comparison of flights with different rate feedback gains (color coded), identical for the experiment and simulation. Solid lines correspond to mean states. Color belts around lines correspond to standard deviation.

titude in simulation, as these measurements should be closer to the real attitude. Finally, due to hand assembly, the robot mechanisms and wings are not perfectly aligned as assumed in the model, and the robot components are to some extent compliant and its mechanisms allow for certain amount of play, unlike in the model.

Nevertheless, the results presented in the previous sections show that these imperfections are of a secondary importance, as the dominant effects, as well as the trends when changing the vehicle (and model) parameters, remained well captured by the simulation.

#### 4.6 Controller improvement for fast forward flight

The model was further used to improve the robot’s control system performance. While the hand-tuned gains gave satisfactory performance in a wide range of body pitch angles, ranging from hover to  $60^\circ$ , the pitch rotation was less well damped at higher body pitch angles (Figure 19). In fact, when attempting to reach the robot’s maximal speed by commanding  $70^\circ$  pitch in combination with full throttle, a divergent pitch oscillation with an amplitude of approximately  $\sim 30^\circ$  and a frequency of  $\sim 1$  Hz would develop (Figure 23).

Despite the fact that this high speed flight condition (body speed to wing velocity ratio  $w/U = 3.5$ ) lies already outside of the validity region of the model, the simulation does predict pitch oscillation of similar magnitude and frequency (Figure 23). In simulation, we could stabilize the robot by increasing the rate feedback gain by a factor of 2.5 (Figure 24). However, it should be noted that the steady state prediction of the model ( $\theta_{SS} = 52^\circ$ ) was already quite different from the average body pitch during the fast forward flight with diverging oscillation of the real robot ( $\theta_{SS} \sim 70^\circ$ ). Nev-

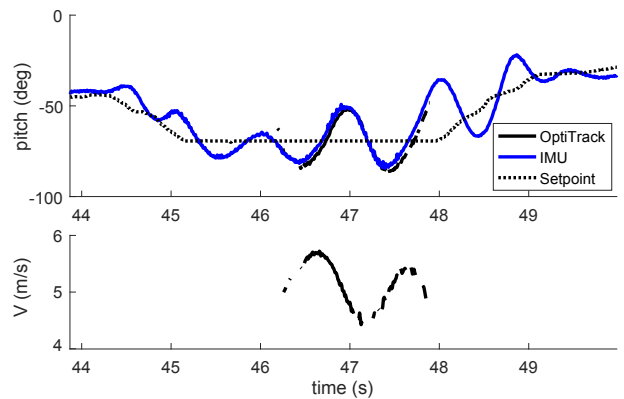


Figure 23: Pitch oscillation developing at full thrust with rate feedback gain of 0.0654. Due to limited tracking volume size only part of the maneuver was captured with the motion capture system.

ertheless, increasing the rate feedback gain in the real robot by the same factor did result in a stable flight and allowed to reach the speed of 6.7 m/s (Figure 25). Speeds of up to 7 m/s were captured in further trials with a second vehicle, not equipped with on-board logging. Videos of the high-speed flights with the original and the adjusted gain can be found online: [https://www.youtube.com/playlist?list=PL\\_KSX9GOn2P8nD6go-RTL9Vp\\_Mb08b5jn](https://www.youtube.com/playlist?list=PL_KSX9GOn2P8nD6go-RTL9Vp_Mb08b5jn).

Thus, the model still captures some of the dynamic behaviour, and can be useful for initial control gain tuning, even outside of the validity region for the linear drag assumption. The gains adjusted for high speed flight still stabilize the robot at hover, although with a slightly worse performance. For maximal performance in any flight regime, a gain scheduling approach could be used to adjust the gains in function of the flight speed.

## 5 CONCLUSIONS AND RECOMMENDATIONS

We have presented a minimal longitudinal dynamic model for a tail-less flapping wing robot, which we validated with flight recordings of a real robot, the DelFly Nimble, for flight conditions ranging from near-hover to cruise forward flight ( $\sim 3.5$  m/s). Moreover, we showed that the model captures well also the effects of varying some of the robot properties, such as the centre of mass location or the controller parameters. Although the model validity is limited only to speeds that are comparable to or lower than the mean wing speed due to flapping ( $\sim 1.7$  m/s), the dynamic trend shown by the model was informative enough to help improve the flight controller even for high speeds, and allowed to achieve stable fast forward flight even at maximum throttle, reaching a speed of 7 m/s.

While the model parameters were identified for a specific robot, the model structure is directly applicable to any flapping wing robots or natural fliers that utilize the mean stroke angle modulation for pitch control, e.g. [6, 45]. Adjusting the

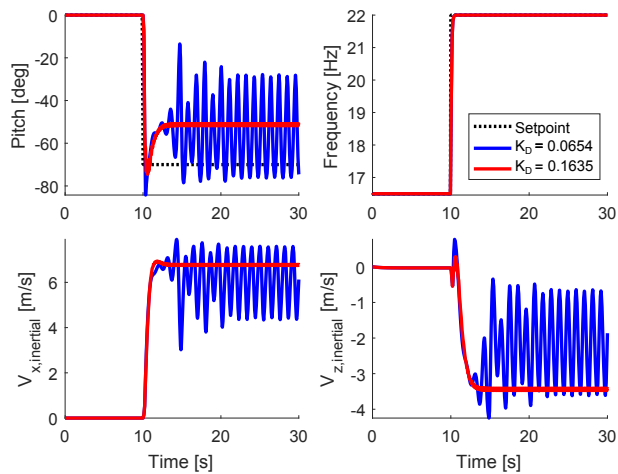


Figure 24: Comparison of effect of different rate feedback gains during a maximum thrust, 70 degree forward pitch setpoint maneuver.

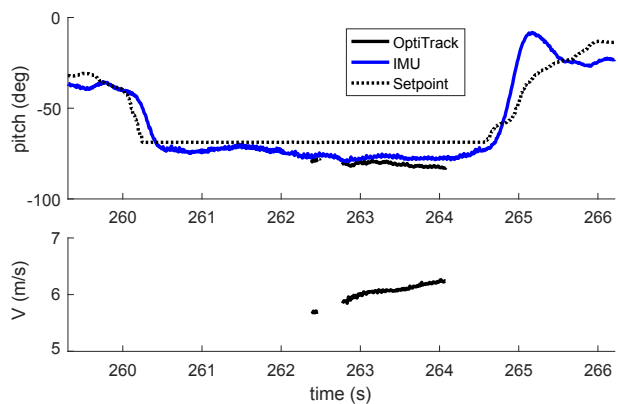


Figure 25: Stable full thrust level flight with rate feedback gain of 0.1635.

model to other means of pitch torque generation, as in [5, 7, 9], is also possible. Further research should look into extending the validity region, possibly by including non-linearity in the cycle averaged drag forces. Following the same approach as in the current work, the model can be extended to 3D by including also the lateral dynamics.

#### ACKNOWLEDGEMENTS

The flight data used for the model validation as well as the simulation model implemented in MATLAB/Simulink are available as open access data at DataverseNL: <https://hdl.handle.net/10411/YPGWY3>.

#### REFERENCES

[1] G. C. H. E. de Croon et al. “Design, aerodynamics, and vision-based control of the DeIFly”. In: *International Journal of Micro Air Vehicles* 1.2 (June 2009), pp. 71–97.

[2] Charles Richter and Hod Lipson. “Untethered Hovering Flapping Flight of a 3D-Printed Mechanical Insect”. In: *Artificial Life* 17.2 (Apr. 2011), pp. 73–86.

[3] Z. E. Teoh et al. “A hovering flapping-wing microrobot with altitude control and passive upright stability”. In: *2012 IEEE/RSJ International Conference on Intelligent Robots and Systems*. IEEE, Oct. 2012, pp. 3209–3216.

[4] Quoc-Viet Nguyen, Woei-Leong Chan, and Marco Debiasi. “An insect-inspired flapping wing micro air vehicle with double wing clap-fling effects and capability of sustained hovering”. In: *Bioinspiration, Biomimetics, and Bioreplication 2015* © 2015 SPIE. Ed. by Akhlesh Lakhtakia, Mato Knez, and Raúl J. Martín-Palma. Mar. 2015.

[5] Matthew Keennon, Karl Klingebiel, and Henry Won. “Development of the Nano Hummingbird: A Tailless Flapping Wing Micro Air Vehicle”. In: *50th AIAA Aerospace Sciences Meeting including the New Horizons Forum and Aerospace Exposition*. January. Reston, Virginia: American Institute of Aeronautics and Astronautics, Jan. 2012, pp. 1–24.

[6] Kevin Y. Ma et al. “Controlled Flight of a Biologically Inspired, Insect-Scale Robot”. In: *Science* 340.6132 (May 2013), pp. 603–607.

[7] David Coleman and Moble Benedict. “On the Development of a Robotic Hummingbird”. In: *54th AIAA Aerospace Sciences Meeting* January (2016), pp. 1–11.

[8] Hoang Vu Phan, Taesam Kang, and Hoon Cheol Park. “Design and stable flight of a 21g insect-like tailless flapping wing micro air vehicle with angular rates feedback control”. In: *Bioinspiration & Biomimetics* 12.3 (Apr. 2017), p. 036006.

[9] A. Roshanbin et al. “COLIBRI: A hovering flapping twin-wing robot”. In: *International Journal of Micro Air Vehicles* March (Mar. 2017), pp. 1–13.

[10] Mao Sun, Ji Kang Wang, and Yan Xiong. “Dynamic flight stability of hovering insects”. In: *Acta Mechanica Sinica* 23.3 (June 2007), pp. 231–246.

[11] Imraan Faruque and Sean J. Humbert. “Dipteran insect flight dynamics. Part 1 Longitudinal motion about hover”. In: *Journal of Theoretical Biology* 264.2 (May 2010), pp. 538–552.

[12] Imraan Faruque and Sean J. Humbert. “Dipteran insect flight dynamics. Part 2: Lateral-directional motion about hover”. In: *Journal of Theoretical Biology* 265.3 (Aug. 2010), pp. 306–313.

- [13] Na Gao, Hikaru Aono, and Hao Liu. “Perturbation analysis of 6DoF flight dynamics and passive dynamic stability of hovering fruit fly *Drosophila melanogaster*”. In: *Journal of Theoretical Biology* 270.1 (Feb. 2011), pp. 98–111.
- [14] Bo Cheng and Xinyan Deng. “Translational and Rotational Damping of Flapping Flight and Its Dynamics and Stability at Hovering”. In: *IEEE Transactions on Robotics* 27.5 (Oct. 2011), pp. 849–864.
- [15] Mao Sun and Ji Kang Wang. “Flight stabilization control of a hovering model insect”. In: *Journal of Experimental Biology* 210.15 (Aug. 2007), pp. 2714–2722.
- [16] Yanlai Zhang and Mao Sun. “Dynamic flight stability of a hovering model insect: lateral motion”. In: *Acta Mechanica Sinica* 26.2 (May 2010), pp. 175–190.
- [17] Xiangdong Zhang and Hao Liu. “A Three-axis PD Control Model for Bumblebee Hovering Stabilization”. In: *Journal of Bionic Engineering* 15.3 (May 2018), pp. 494–504.
- [18] Toshiyuki Nakata et al. “A simulation-based study on longitudinal gust response of flexible flapping wings”. In: *Acta Mechanica Sinica* (Aug. 2018), pp. 1–13.
- [19] Anh Tuan Nguyen and Jae-Hung Han. “Wing flexibility effects on the flight performance of an insect-like flapping-wing micro-air vehicle”. In: *Aerospace Science and Technology* 79 (Aug. 2018), pp. 468–481.
- [20] Sanjay P. Sane and Michael H. Dickinson. “The aerodynamic effects of wing rotation and a revised quasi-steady model of flapping flight.” In: *The Journal of experimental biology* 205.Pt 8 (Apr. 2002), pp. 1087–1096.
- [21] Xinyan Deng et al. “Flapping flight for biomimetic robotic insects: part I-system modeling”. In: *IEEE Transactions on Robotics* 22.4 (Aug. 2006), pp. 776–788.
- [22] Matěj Karásek and André Preumont. “Flapping Flight Stability in Hover: A Comparison of Various Aerodynamic Models”. In: *International Journal of Micro Air Vehicles* 4.3 (Sept. 2012), pp. 203–226.
- [23] Sophie F. Armanini et al. “Quasi-steady aerodynamic model of clap-and-fling flapping MAV and validation using free-flight data”. In: *Bioinspiration & Biomimetics* 11.4 (June 2016), pp. 1–25.
- [24] Mostafa R. A. Nabawy and William J. Crowther. “A Quasi-Steady Lifting Line Theory for Insect-Like Hovering Flight”. In: *PLOS ONE* 10.8 (Aug. 2015). Ed. by Sharon Swartz, e0134972.
- [25] Mostafa R. A. Nabawy and William J. Crowther. “The role of the leading edge vortex in lift augmentation of steadily revolving wings: a change in perspective”. In: *Journal of The Royal Society Interface* 14.132 (July 2017), p. 20170159.
- [26] Loan Thi Kim Au, Hoang Vu Phan, and Hoon Cheol Park. “Comparison of Aerodynamic Forces and Moments Calculated by Three-dimensional Unsteady Blade Element Theory and Computational Fluid Dynamics”. In: *Journal of Bionic Engineering* 14.4 (Oct. 2017), pp. 746–758.
- [27] Xinyan Deng, Luca Schenato, and S. S. Sastry. “Flapping flight for biomimetic robotic insects: part II-flight control design”. In: *IEEE Transactions on Robotics* 22.4 (Aug. 2006), pp. 789–803.
- [28] Christopher T. Orlowski and Anouck R. Girard. “Dynamics, stability, and control analyses of flapping wing micro-air vehicles”. In: *Progress in Aerospace Sciences* 51 (May 2012), pp. 18–30.
- [29] Yan Xiong and Mao Sun. “Stabilization control of a bumblebee in hovering and forward flight”. In: *Acta Mechanica Sinica* 25.1 (Feb. 2009), pp. 13–21.
- [30] Floris van Breugel, William Regan, and Hod Lipson. “From insects to machines”. In: *IEEE Robotics & Automation Magazine* 15.4 (Dec. 2008), pp. 68–74.
- [31] L. Ristroph et al. “Active and passive stabilization of body pitch in insect flight”. In: *Journal of The Royal Society Interface* 10.85 (2013), pp. 20130237–20130237.
- [32] Matěj Karásek et al. “A tailless aerial robotic flapper reveals that flies use torque coupling in rapid banked turns”. In: *Science* 361.6407 (Sept. 2018), pp. 1089–1094.
- [33] G.C.H.E. de Croon et al. *The DelFly*. Dordrecht: Springer Netherlands, 2016, p. 221.
- [34] *Lisa/MXS v1.0 - PaparazziUAV*. [https://wiki.paparazziuav.org/wiki/Lisa/MXS\\_v1.0](https://wiki.paparazziuav.org/wiki/Lisa/MXS_v1.0). Accessed: 2019-01-07.
- [35] J V Caetano et al. “Error analysis and assessment of unsteady forces acting on a flapping wing micro air vehicle: free flight versus wind-tunnel experimental methods”. In: *Bioinspiration & Biomimetics* 10.5 (Oct. 2015), p. 056004.
- [36] Charles P Ellington. “The aerodynamics of hovering insect flight. IV. Aerodynamic Mechanisms”. In: *Philosophical Transactions of the Royal Society of London. Series B, Biological Sciences* 305.1122 (1984), pp. 79–113.
- [37] Robert Stengel. *Flight dynamics*. Princeton, NJ : Princeton University Press, 2004, p. 169.

- [38] Yanghai Nan et al. “Experimental optimization of wing shape for a hummingbird-like flapping wing micro air vehicle”. In: *Bioinspiration & Biomimetics* 12.2 (Mar. 2017), p. 026010.
- [39] Matt R. Jardin and Eric R. Mueller. “Optimized Measurements of Unmanned-Air-Vehicle Mass Moment of Inertia with a Bifilar Pendulum”. In: *Journal of Aircraft* 46.3 (May 2009), pp. 763–775.
- [40] A. Roshanbin et al. “COLIBRI: A hovering flapping twin-wing robot”. In: *International Journal of Micro Air Vehicles* 9.4 (2017), pp. 270–282.
- [41] M. Sun. “Dynamic flight stability of a hovering bumblebee”. In: *Journal of Experimental Biology* 208.3 (2005), pp. 447–459.
- [42] Michael H. Dickinson and Florian T. Muijres. “The aerodynamics and control of free flight manoeuvres in *Drosophila*”. In: *Philosophical Transactions of the Royal Society B: Biological Sciences* 371.1704 (Sept. 2016), p. 20150388.
- [43] Bo Cheng et al. “Flight mechanics and control of escape manoeuvres in hummingbirds. II. Aerodynamic force production, flight control and performance limitations.” In: *The Journal of experimental biology* 219.Pt 22 (Nov. 2016), pp. 3532–3543.
- [44] J. Kennedy and R. Eberhart. “Particle swarm optimization”. In: *IEEE International Conference on Particle swarm optimization*. Vol. 4. IEEE, 1995, pp. 1942–1948.
- [45] Florian T. Muijres et al. “Flies Evade Looming Targets by Executing Rapid Visually Directed Banked Turns”. In: *Science* 344.6180 (Apr. 2014), pp. 172–177.